PCCP

RSC Publishing

PAPER

View Article Online
View Journal | View Issue

Cite this: *Phys. Chem. Chem. Phys.*, 2013, **15**, 16127

Effects of cross-sectional area on the tunneling-junction array in octahedral PbSe colloidal-nanocrystal solids

Shao-Chien Chiu,[a] Jia-Sin Jhang,[a] Jenn-Fang Chen,[a] Jiye Fang[b] and Wen-Bin Jian*[a]

Received 17th May 2013,
Accepted 23rd July 2013

DOI: 10.1039/c3cp52083h

www.rsc.org/pccp

Octahedral PbSe colloidal nanocrystals (NCs) are used to assemble a solid. Because of the special feature of the apexes of the octahedrons, the cross-sectional area of the inter-dot tunneling junctions is much smaller than that formed between spherical NCs. The inter-dot separation between NCs is easily adjusted by mild thermal treatment. Like a spherical NC-solid, the resistance of the octahedral NC-solid is exponentially dependent on the inter-dot separation. On the contrary, due to the difference in the cross-sectional area between the NCs, electron transport in the octahedral NC-solid does not follow the same model used for the explanation of electron transport in a spherical NC-solid. Through analyses of current–voltage and resistance–temperature behaviors, we have confirmed that the model of fluctuation-induced tunneling conduction fits very well with all of the data and explains the variation in the electrical properties of octahedral PbSe colloidal NC-solids after thermal annealing.

Introduction

Colloidal nanocrystal (NC) solids, which are alternatively named granular metals, have varied electrical properties, which depend on shape, size, packing, and separation between the NCs.[1] More specifically, the separation can be tuned to change the tunneling junction between NCs. If the separation is tuned to be shorter, the NC-solid exhibits a metallic property. In contrast, the NC-solid exhibits an insulating property with a longer separation between NCs. The tuning of the gap separation between NCs leads to a metal-to-insulator transition in NC-solids. This particular property demonstrates that the tunneling junctions between, rather than the intrinsic materials of, the NCs play the decisive role in electron transport.

The application of NC-solids has been demonstrated in modern electronic devices, such as carrier multiplication devices,[2] memory devices,[3] field-effect transistors,[4] thermoelectric devices,[5] sensitive photodetectors,[6] and light-emitting diodes.[7] Carrier transport in NC-solids is highly adjustable. For example, both diffusive and drift motions of carries occur, and the diffusion process may be excluded to promote the response speed of photodetectors.[6] Through control of the inter-dot spacing, which was tuned over a range of 1.3 nm, a NC light-emitting diode can be operated with high radiance and quantum efficiencies.[7] All of these experimental results indicate that the manipulation of the inter-dot spacing and tunneling junctions between NCs is essential for the device performance.

NCs with a spherical shape are commonly used for device fabrication and, as a consequence, electron transport in spherical NC-solids has been extensively studied. It has been argued that electron transport in spherical NC-solids follows the models of nearest neighbor hopping, Mott's variable range hopping (VRH), or Efros–Schklovskii (ES) hopping for different NC materials in specific temperature windows.[8,9] The diversity of transport mechanisms may originate from the tunneling process between NCs. The cross-sectional area of the tunneling junction between spherical NCs is large, thus charge carriers are capable of hopping both to neighboring and to far away NCs. Charge carriers that hop far away are in search of another carrier that has an energy state similar to theirs, this particular transport process is named Mott's VRH conduction. If the cross-sectional area is reduced so that it is much smaller, the electron transport in the NC-solid deviates away from the above-mentioned models. In this paper, we demonstrate that a different model can be used to describe electron transport in NC-solids and compare data with results obtained from studies on spherical NC-solids. Octahedral NCs were used to demonstrate the unique transport behavior that results from the shrinkage of the cross-sectional area of the tunneling junction between NCs.

Experimental

Octahedral PbSe NCs (inset to Fig. 1(a)) capped with oleic acid and trioctylphosphine were synthesized by a high-temperature organic solution approach and were stocked in hexane. The octahedral

[a] *Department of Electrophysics, National Chiao Tung University, Hsinchu 30010, Taiwan. E-mail: wbjian@mail.nctu.edu.tw*
[b] *Department of Chemistry, State University of New York at Binghamton, Binghamton, New York 13902-6000, USA*

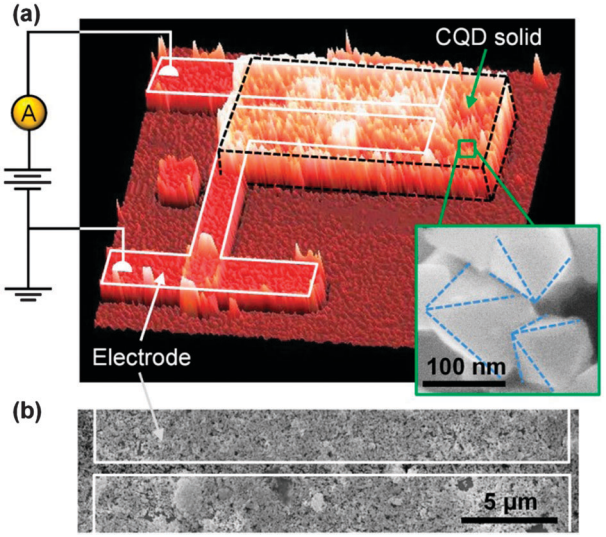

Fig. 1 A three-dimensional representation and the original two-dimensional SEM image are displayed in (a) and (b). The circuit diagram for the electrical measurements is given in (a), where the metal electrodes and the NC-solid are indicated by solid lines in white and by dashed lines in black, respectively. The inset to (a) shows a magnification of the SEM image of individual PbSe NCs where the octahedral shape is emphasized by dashed lines in blue.

PbSe NCs were size-selected from the products prepared according to a method described in ref. 10, and it was determined that the content of Mn in these octahedral PbSe NCs are insignificant and can be neglected. The average size, which is defined as the longest distance between two apexes of an octahedron, is about 122 ± 18 nm. Using both electron-beam lithography and thermal evaporation, a Si wafer substrate was patterned with a pair of 20 nm thick Pt electrodes with a trench gap of 1 μm in width. The Pt electrodes were connected to large, photolithographically pre-patterned Ti/Au electrodes. The substrate was spin-coated with a PMMA thin film and reprocessed by electron-beam lithography patterning to open a window directly on top of the trench gap. The PbSe NC dispersion was drop cast onto the PMMA protected substrate. PbSe NCs self-assembled on both the PMMA protected and open surfaces. The substrate was dried in air and then immersed in acetone for 1 h to remove the PMMA protection and the excess of PbSe NCs. Thereafter, the substrate was dried under a flow of nitrogen gas. The octahedral PbSe NCs assembled to form a piece of micrometer sized bulk material with dimensions of 25 μm in length, 1 μm in width, and 1 μm in thickness, sitting in the trench gap between the Pt electrodes as shown in Fig. 1. The thickness of the NC bulk material was determined with an atomic force microscope (AFM, Seiko Instruments Inc. SPA-300HV).

The resistance of the as-fabricated device was higher than 10^{12} Ω at room temperature, implying a large inter-dot separation, which hinders the electron tunneling process between the NCs and causes an insulating effect. The NC-solid intrinsically gives an ultra-high resistance so the contact issue is insignificant.[11] In addition, the long trench structure provides a large contact area thus reducing the contact resistance. Post-annealing was then carried out on the as-made sample. Annealing was performed at either 225 or 250 °C in a high vacuum for 10–360 min in order to partially remove the capping agents from the surface of the PbSe NCs. After annealing, the device was examined with a scanning electron microscope (SEM, JEOL JSM-6700F) to ensure that the morphology of the octahedral PbSe NCs was complete, without any features of melting. Fig. 1(b) presents a top-view SEM image of the whole area of the NC-solid device. The device was finally loaded into either an insert cryostat (Variable Temperature Insert Cryostat) or a closed cycle system (REF-16950-DC) from CRYO Industries of America Inc. for measurements of current–voltage (*I–V*) curves at various temperatures. The *I–V* measurement was carried out by using a Keithley 6430. The circuit connection is also given in Fig. 1(a).

The resistance was estimated from a linear least-square fit to the *I–V* curve in a small bias voltage range between 10 and −10 mV.

Results and discussion

The resistance of the NC-solid decreases with an increasing temperature and post-annealing time. Fig. 2(a) and (b) display the annealing time and temperature dependencies, respectively. For the same annealing temperature, the room-temperature resistance of the NC-solid decreases after annealing for a longer time. The resistance changes by four orders of magnitude after the NC-solid is annealed at 225 °C for 45 min (Fig. 2(a)). In addition, raising the annealing temperature causes a much larger drop in the resistance. For the same annealing time of 10 min, the 225 °C-annealed NC-solid shows a room-temperature resistance one thousand times smaller, whereas the 250 °C-annealed one shows a value ten million times smaller, than the as-made NC-solid. The inset to Fig. 2(b) shows that PbSe NCs do not melt during thermal treatment. The result also hints at a reduction of inter-dot separation that originates from the partial removal of the capping agents on the surface of the PbSe NCs.

Fig. 3(a) presents typical *I–V* curves for the 225 °C-annealed NC-solid. It is noted that neither zero current nor threshold

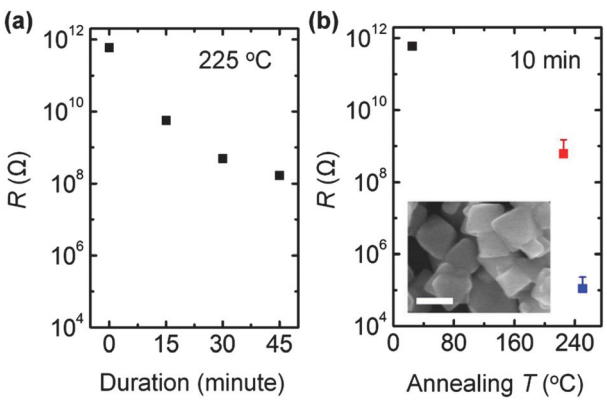

Fig. 2 (a) The room-temperature resistance as a function of annealing time for the PbSe NC-solid annealed at 225 °C. (b) The room-temperature resistance of PbSe NC-solids at various annealing temperatures for 10 min. The inset shows an SEM image with a scale bar of 100 nm of the 250 °C-annealed PbSe NC-solid.

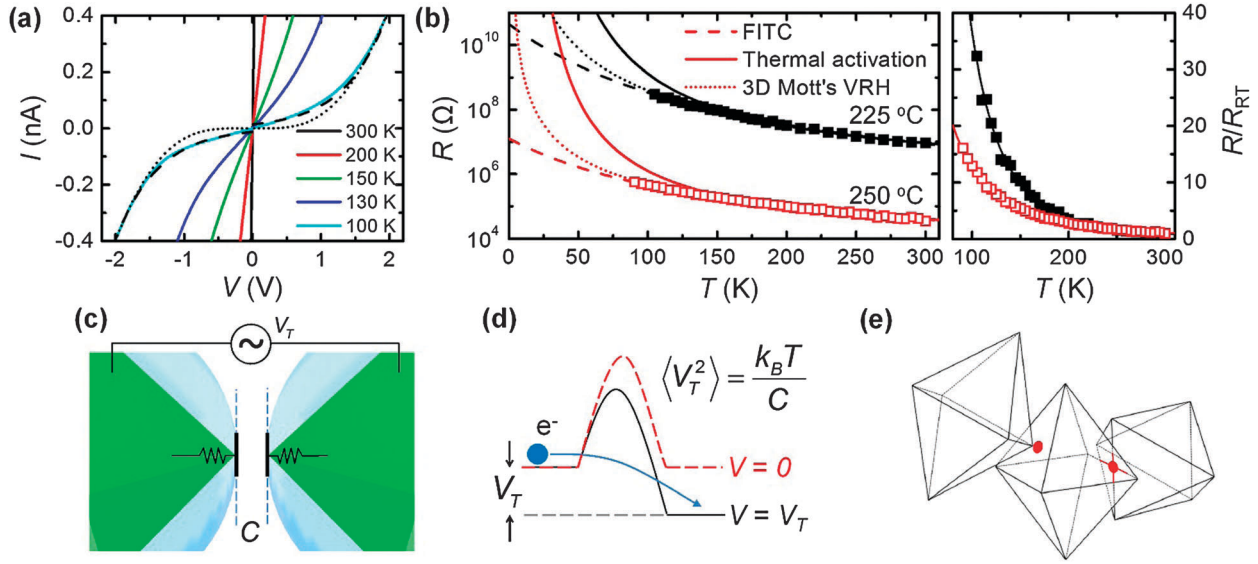

Fig. 3 (a) *I–V* curves of the PbSe NC-solid after annealing at 225 °C for 10 min. The dashed and dotted lines present the best fits from the models of FITC and 3D Mott's VRH conduction, respectively. (b) The left panel presents temperature dependent resistances of the NC-solids annealed at 225 °C for 30 min and at 250 °C for 10 min, represented by closed and open squares. The dashed, dotted, and solid lines present the best fits to the theoretical models of FITC, Mott's 3D VRH, and thermally activated conduction, respectively. The right panel presents the temperature dependence of the resistance divided by its value at room temperature. (c) Scheme of the junction proposed by the FITC model between two neighboring NCs. The thermal fluctuation voltage, which is built up by thermally excited electrons, and the inter-dot capacitance are marked on the scheme. (d) Scheme of the potential barrier across the junction between two neighboring NCs. (e) A possible configuration between two octahedral PbSe NCs that could lead to an ultra-small capacitance and to raise the thermal fluctuation voltage.

voltage can be identified on the *I–V* curves at temperatures from 100 to 300 K. This indicates a different type of behavior to that of the collective Coulomb blockade effect,[12] which has been observed and studied for spherical PbSe NCs of ~14.6 nm in average diameter.[13] To further investigate the electron transport in octahedral NCs, the typical temperature behavior of resistance is portrayed in Fig. 3(b) and is analyzed by using the models of three-dimensional (3D) Mott's VRH,[14] thermal activation, and Sheng's fluctuation-induced tunneling conduction (FITC).[15] The equations of $R(T) \propto \exp((T_0'/T)^{1/4})$ and $R(T) \propto \exp(E_A/k_BT)$ are used for the models of 3D Mott's VRH (dotted lines in Fig. 3(b)) and thermal activation (solid lines in Fig. 3(b)) to describe the temperature dependent resistance, where k_B is the Boltzmann constant, and T_0' and E_A are parameters. The temperature behaviour of resistance agrees well with the FITC model (dashed lines in Fig. 3(b)) according to the equation of $R(T) = R_0 \exp(T_1/(T + T_0))$, where R_0 is a constant, and T_0 and T_1 are two parameters. For fittings to the FITC, the thermal activation, and the Mott's 3D VRH models, the standard deviations of the 225 °C-annealed NC-solid are 6.4×10^6, 1.5×10^8, and 1.0×10^7 Ω and those of the 250 °C-annealed NC-solid are 5.0×10^3, 3.4×10^5, and 1.4×10^4 Ω, respectively. The fitting to the FITC model gives the smallest standard deviation. More than five 225 °C-annealed and six 250 °C-annealed samples show consistently the same fitting results. The right panel of Fig. 3(b) emphasizes the difference in temperature behaviors for the data shown on the left. The variation of temperature behaviors will be discussed later. Further, the FITC model predicts *I–V* behavior that precisely fits to the data (the dashed line in Fig. 3(a)) while the 3D Mott's VRH model cannot effectively describe the voltage dependent behavior (see the dotted fitting line).

As pointed out in the introduction, electron transport in NC-solids is mainly dependent on the inter-dot tunneling process. Fig. 3(c) is an illustration of the inter-dot tunneling junction. For spherical NCs (indicated by the area in light blue), the cross-sectional area of the tunneling junction is large. The capacitance of the inter-dot junction drops when the cross-sectional area of the tunneling junction shrinks (see the green area in Fig. 3(c)). Because the thermal fluctuation voltage V_T is inversely proportional to the inter-dot capacitance, thermally excited electrons build up a high V_T between NCs. The V_T lowers the potential barrier between the NCs (Fig. 3(d)) and drives a high current tunneling through. The scenario of a shrinking cross-section of the tunneling junction is described by the FITC model. The reduction of the junction area can easily be achieved and realized by using octahedral NCs as schematically illustrated in Fig. 3(e). The experimental data presented in Fig. 3(b) can be rationalized progressively. Annealing at a higher temperature removes more capping molecules from the surface of the NCs and causes a reduction of the inter-dot separation. Thus inducing a decrease in the resistance of the NC-solid and an increase in the inter-dot capacitance. According to a simple parallel-plate model of capacitance, the inter-dot capacitance is inversely proportional to the inter-dot separation. Because the increasing capacitance curtails the thermal fluctuation voltage, the ratio of resistance variation diminishes (open squares in the right panel in Fig. 3(b)).

The similarities and differences of the electrical properties between octahedral and spherical NCs are summarized in Fig. 4.

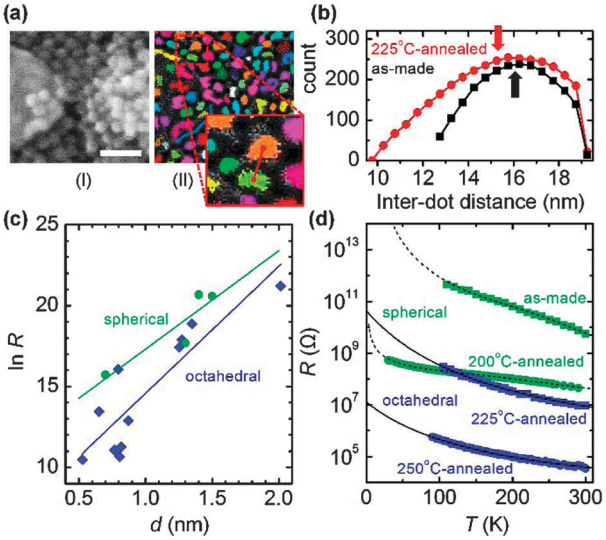

Fig. 4 (a) SEM image with a scale bar of 50 nm (I) and the corresponding spherical NCs marked as colored areas (II). The inset demonstrates the method for determination of the center-to-center distance between NCs. (b) Statistical distribution of the center-to-center distance between the NCs for the as-made and the 225 °C-annealed NCs. The arrows point to the average values of the center-to-center distance between the NCs. (c) The logarithm of resistance as a function of the inter-dot separation between NCs. The data of octahedral and spherical PbSe NCs are represented by blue diamonds and green spheres, respectively. The solid lines represent the results of linear least-square fittings. (d) Data of temperature dependent resistances and fittings to theoretical models of the as-made and 200 °C-annealed spherical PbSe NCs (in green), and the 225 °C-annealed and 250 °C-annealed octahedral PbSe NCs (in blue).

Because the spherical NCs are small, the inter-dot distance can be evaluated from the SEM images. Fig. 4(a) presents the method to obtain the center-to-center distance between NCs. The statistical distribution of the center-to-center distance (Fig. 4(b)) gives the average value, the inter-dot separation distance (d) can be calculated by subtracting the average diameter ($\sim$14.6 nm). On the other hand, the octahedral NCs are rather large, thus the two T_0 and T_1 parameters evaluated by the FITC model, are used to calculate the inter-dot separation (d), and hence the resistance on a logarithmic scale as a function of the inter-dot separation is shown in Fig. 4(c) for octahedral NCs. The inter-dot separation is calculated using $\hbar\pi^{-1}(T_1/T_0)(mV_0/2)^{-1/2}$, where m is the mass of an electron and the tunneling barrier V_0 is 4.56 eV.[16] Data from spherical NCs[13,17] are shown in Fig. 4(c) for comparison.

The resistances of both octahedral and spherical NC-solids are strongly dependent on d in agreement with $R(T) \propto \exp(2kd)$, and the k values of 4×10^9 and 3×10^9 m^{-1} are extracted from fittings to the data of the octahedral and spherical NC-solids. The estimated k values are very close to the ideal magnitude of $k = \hbar^{-1}(2mV_0)^{1/2} = 1.1 \times 10^{10}$ m^{-1} for tunneling transport between NCs. On the other hand, the large variations in the cross-sectional areas cause different electron transport processes to occur and lead to different temperature behaviors (see Fig. 4(d)). The electron transport in octahedral NCs follows the FITC model while that in spherical NCs follows the VRH conduction model.[17] The octahedral PbSe NCs are larger, while the spherical NCs are smaller than the exciton Bohr radius of PbSe. The quantum confinement energies of the octahedral and the spherical NCs are about 5 and 160 meV, respectively. The quantum confinement effect in octahedral NC-solids is thus negligibly small. In contrast, the quantum confinement effect in spherical NC-solids is large thus it may need to be considered. The common observation of VRH conduction may be in correlation with the strong quantum effect. On the other hand, the electron transport mechanism in the NC-solid is more dependent on the inter-dot junction than on the NC composition thus the effect of quantum confinement may not be the only decisive factor in electron transport in NC-solids.

Conclusions

In summary, we probed electron transport in the tunneling-junction array in octahedral PbSe NC-solids. The special shape of octahedral NCs causes the formation of an ultra-small cross-section at the inter-dot tunneling junction. Like with spherical NC-solids, the resistance of the octahedral NC-solid is exponentially dependent on the inter-dot separation, which can be tuned by mild thermal annealing. Unlike spherical NC-solids, the octahedral NC-solid exhibits a different behavior of electron transport owing to a smaller cross-sectional area at the inter-dot tunneling junction. The FITC model adequately predicts the data of the I–V and R–T curves of the PbSe octahedral NC-solid and explains the resistance drop and the reduction of the thermal fluctuation voltage after post-annealing.

Acknowledgements

This work was supported by the Taiwan National Science Council under Grant Numbers NSC100-2112-M-009-017-MY3 and by the MOE ATU Program.

Notes and references

1 I. S. Beloborodov, A. V. Lopatin, V. M. Vinokur and K. B. Efetov, *Rev. Mod. Phys.*, 2007, **79**, 469.
2 R. D. Schaller and V. I. Klimov, *Phys. Rev. Lett.*, 2004, **92**, 186601.
3 M. D. Fischbein and M. Drndic, *Appl. Phys. Lett.*, 2005, **86**, 193106.
4 D. V. Talapin and C. B. Murray, *Science*, 2005, **310**, 86–89.
5 R. Y. Wang, J. P. Feser, J. S. Lee, D. V. Talapin, R. Segalman and A. Majumdar, *Nano Lett.*, 2008, **8**, 2283–2288.
6 J. P. Clifford, G. Konstantatos, K. W. Johnston, S. Hoogland, L. Levina and E. H. Sargent, *Nat. Nanotechnol.*, 2009, **4**, 40–44.
7 L. Sun, J. J. Choi, D. Stachnik, A. C. Bartnik, B.-R. Hyun, G. G. Malliaras, T. Hanrath and F. W. Wise, *Nat. Nanotechnol.*, 2012, **7**, 369–373.
8 T. Mentzel, V. Porter, S. Geyer, K. MacLean, M. G. Bawendi and M. Kastner, *Phys. Rev. B: Condens. Matter Mater. Phys.*, 2008, **77**, 075316.
9 H. Liu, A. Pourret and P. Guyot-Sionnest, *ACS Nano*, 2010, **4**, 5211–5216.

10 W. Lu, P. Gao, W. B. Jian, Z. L. Wang and J. Fang, *J. Am. Chem. Soc.*, 2004, **126**, 14816–14821.
11 Y. F. Lin, T. H. Chen, C. H. Chang, Y. W. Chang, Y. C. Chiu, H. C. Hung, J. J. Kai, Z. Liu, J. Fang and W. B. Jian, *Phys. Chem. Chem. Phys.*, 2010, **12**, 10928–10932.
12 A. A. Middleton and N. S. Wingreen, *Phys. Rev. Lett.*, 1993, **71**, 3198–3201.
13 Y. C. Ou, J. J. Wu, J. Fang and W. B. Jian, *J. Phys. Chem. C*, 2009, **113**, 7887–7891.
14 N. Mott, *Conduction in Non-Crystalline Materials*, Clarendon Press, Oxford, 1993.
15 P. Sheng, E. K. Sichel and J. I. Gittleman, *Phys. Rev. Lett.*, 1978, **40**, 1197–1200.
16 J. Jasieniak, M. Califano and S. E. Watkins, *ACS Nano*, 2011, **5**, 5888–5902.
17 Y. F. Lin, S. C. Chiu, S. T. Wang, S. K. Fu, C. H. Chen, W. J. Xie, S. H. Yang, C. S. Hsu, J. F. Chen and X. Zhou, *Electrophoresis*, 2012, **33**, 2475–2481.